Chemical Science

Cite this: *Chem. Sci.*, 2012, **3**, 2868

www.rsc.org/chemicalscience

EDGE ARTICLE

Hysteresis in the ground and excited spin state up to 10 T of a $[Mn^{III}_6Mn^{III}]^{3+}$ triplesalen single-molecule magnet†

Veronika Hoeke,[a] Klaus Gieb,[b] Paul Müller,[b] Liviu Ungur,[c] Liviu F. Chibotaru,[c] Maik Heidemeier,[a] Erich Krickemeyer,[a] Anja Stammler,[a] Hartmut Bögge,[a] Christian Schröder,[d] Jürgen Schnack[e] and Thorsten Glaser*[a]

Received 22nd May 2012, Accepted 18th June 2012
DOI: 10.1039/c2sc20649h

We have synthesized the triplesalen-based single-molecule magnet (SMM) $[Mn^{III}_6Mn^{III}]^{3+}$ as a variation of our SMM $[Mn^{III}_6Cr^{III}](BPh_4)_3$. The use of the rod-shaped anion lactate (lac) was intended to enforce a rod packing and resulted in the crystallization of $[Mn^{III}_6Mn^{III}](lac)_3$ in the highly symmetric space group $R\bar{3}$. This entails a crystallographic S_6 symmetry of the $[Mn^{III}_6Mn^{III}]^{3+}$ molecules, which in addition are all aligned with the crystallographic *c* axis. Moreover, the molecular environment of each $[Mn^{III}_6Mn^{III}]^{3+}$ molecule is highly symmetric. Single-crystals of $[Mn^{III}_6Mn^{III}](lac)_3$ exhibit a double hysteresis at 0.3 K with a hysteretic opening not only for the spin ground state up to 1.8 T, but also for an excited state becoming the ground state at $\approx$ 3.4 T with a hysteretic opening up to 10 T. *Ab initio* calculations including spin-orbit coupling establish a non-magnetic behavior of the central Mn^{III} low-spin (l.s.) ion at low temperatures, demonstrating that predictions from ligand-field theory are corroborated in the case of Mn^{III} l.s. by *ab intio* calculations. Simulations of the field- and temperature-dependent magnetization data indicate that $[Mn^{III}_6Mn^{III}]^{3+}$ is in the limit of weak exchange ($J \ll D$) with antiferromagnetic interactions in the trinuclear Mn^{III}_3 triplesalen subunits resulting in intermediate $S^* = 2$ spins. Slight ferromagnetic interactions between the two trinuclear Mn^{III}_3 subunits lead to a ground state in zero-field that is approximately described by a total spin quantum number $S = 4$. This ground state exhibits only a very small anisotropy barrier due to the misalignment of the local zero-field splitting tensors. At higher magnetic fields of $\approx$ 3.4 T, the spin configuration changes to an all-up orientation of the local Mn^{III} spins, with the main part of the Zeeman energy needed for the spin-flip being required to overcome the local Mn^{III} anisotropy barriers, while only minor contributions of the Zeeman energy are needed to overcome the antiferromagnetic interactions. These combined theoretical analyses provide a clear picture of the double-hysteretic behavior of the $[Mn^{III}_6Mn^{III}]^{3+}$ single-molecule magnet with hysteretic openings up to 10 T.

Introduction

SMMs are a class of coordination compounds that exhibit a hysteresis of the magnetization which is of a purely molecular origin.[1–5] This phenomenon is related to a slow relaxation of the magnetization due to an energy barrier for spin reversal arising from the combination of a high spin ground state S_t and a strong magnetic anisotropy D_{S_t}. Besides allowing for the direct observation of quantum effects, these bistable molecules attract attention due to their potential applications in information storage and quantum computing.[6–14]

There are two mechanisms to overcome the anisotropy barrier. On the one hand, there is a thermal pathway over the top of the barrier. Thus, a high anisotropy barrier is important to slow down the magnetization relaxation. On the other hand, SMMs may also tunnel through the anisotropy barrier. The tunneling probability *p* scales with $p \propto 1 - \exp(E/D)^S$. Thus, a high spin *S* of zero

[a]*Fakultät für Chemie, Universität Bielefeld, D-33615 Bielefeld, Germany. E-mail: thorsten.glaser@uni-bielefeld.de*
[b]*Physikalisches Institut III, Universität Erlangen-Nürnberg, D-91058 Erlangen, Germany*
[c]*Division of Quantum and Physical Chemistry, Katholieke Universiteit Leuven, B-3001 Heverlee, Belgium*
[d]*Fachbereich Ingenieurwissenschaften und Mathematik, Fachhochschule Bielefeld, D-33602 Bielefeld, Germany*
[e]*Fakultät für Physik, Universität Bielefeld, D-33615 Bielefeld, Germany*

† Electronic supplementary information (ESI) available: Thermal ellipsoid plots (Fig. S1) and selected bond distances and angles (Table S1) for **1**, structures of the calculated fragments in approximations A–D of the *ab initio* calculations (Fig. S2 and S3) and descriptions of the supplementary movies. Four movies in avi format illustrating classical spin dynamics simulations. CCDC reference numbers 883027. For ESI and crystallographic data in CIF or other electronic format see DOI: 10.1039/c2sc20649h

rhombicity, *i.e.* $E/D = 0$, is key to minimizing the magnetization tunneling.[15] This implies that a high anisotropy barrier for a small rhombic spin cannot increase the blocking temperature T_B, *i.e.* the temperature for a specific experimental technique that allows the observation of slow magnetization relaxation.

In order to combine a high spin ground state with no rhombicity, we have designed the C_3 symmetric ligand system triplesalen, which combines the phloroglucinol bridging unit for high spin ground states by the spin-polarization mechanism[16–20] with a salen-like ligand environment for single-site magnetic anisotropies by a strong tetragonal ligand field.[20–24] The C_3 symmetry of the ligand should result in C_3 symmetric complexes which have by symmetry a rhombicity $E/D = 0$. The trinuclear complexes of the triplesalen ligand $[(talen^{t\text{-}Bu_2})M^t_3]^{m+}$ (**A**, Scheme 1) are indeed C_3 symmetric and exhibit a bowl-shaped molecular structure[22,25] which preorganizes the axial coordination sites of the metal–salen subunits for the complementary binding of three facial nitrogen atoms of a hexacyanometallate (**B**), thus allowing for the formation of heptanuclear complexes $\mathbf{[M^t_6M^c]^{n+}}$ by molecular recognition of three building blocks. Hence, we were able to synthesize $\mathbf{[Mn^{III}_6Cr^{III}]^{3+}}$, which is an SMM with $S_t = 21/2$.[26] The anisotropy barrier U^{eff} was determined from AC measurements to be 25.4 K and the blocking temperature from single-crystal magnetization measurements to be ≈ 1.5 K. The molecular recognition of the three building blocks to form $\mathbf{[M^t_6M^c]^{n+}}$ results in a driving force for its formation[24] that allows us to modify the building blocks without losing their tendency to assemble to heptanuclear entities.[27,28] Thus, we can rationally refine this system of SMMs, which appears to us as a key advantage.

A successful strategy to increase the blocking temperature T_B is the incorporation of metal ions with a strong intrinsic magnetic anisotropy.[29–36] As this anisotropy originates from orbital contributions to the magnetic moment, we employed $[Mn^{III}(CN)_6]^{3-}$ (d^4 l.s., $^3T_{1g}$ ground state in O_h) which possesses a first-order orbital angular momentum.[37–43] We present here the new SMM $\mathbf{[Mn^{III}_6Mn^{III}]^{3+}}$ that exhibits a hysteresis not only in the ground state but also in an excited state, which becomes ground state at high magnetic fields.

Results and discussion

Synthesis and characterization

We have reported several $\mathbf{[Mn^{III}_6M^c]^{3+}}$ complexes ($M^c = Cr^{III}$,[26] Fe^{III},[27] Co^{III} [28]) using various counterions like BPh_4^-,[26] $[Fe^{III}(CN)_6]^{3-}$,[27] PF_6^-, and OAc^-.[28] These compounds crystallize in monoclinic space groups with random orientations of the $\mathbf{[Mn^{III}_6M^c]^{3+}}$ complexes in the crystal structure. These crystal structures have two drawbacks for the SMM behavior of our $\mathbf{[M^t_6M^c]^{n+}}$ SMMs: (1) The molecular structure is not rigorously C_3 symmetric, as no crystallographic C_3 axis (not available in monoclinic space groups) goes through the molecule. (2) The randomness of the molecular environment further reduces the molecular symmetry, especially by stray fields originating from neighboring high spin molecules.

In order to align the C_3 axes of the $\mathbf{[Mn^{III}_6Mn^{III}]^{3+}}$ molecules in the crystal, we have employed in this work the rod-shaped anion lactate. This was inspired by the frequent occurrence of hexagonal and cubic packings in systems with rod-shaped components.[44–48] Reaction of $H_6talen^{t\text{-}Bu_2}$ with $Mn^{II}(OAc)_2\cdot 4H_2O$, $K_3[Mn^{III}(CN)_6]$, and D,L-Na(lac) (lac = lactate) in a methanol/water mixture, followed by slow evaporation of the solvent, led to the formation of brown crystals of two different morphologies, namely hexagonal plates and trigonal prisms. Single-crystal X-ray diffraction analysis of the hexagonal plates resulted in the formulation as $[\{(talen^{t\text{-}Bu_2})(Mn^{III}(MeOH))_3\}_2\{Mn^{III}(CN)_6\}](lac)_3\cdot 10.5MeOH$ (**1**) crystallizing in the hexagonal space group $R\bar{3}$,while the trigonal prisms were attributed to a cubic modification. In the course of our efforts to establish distinct protocols leading to either of the two modifications, we obtained numerous batches consisting of hexagonal plates only, as judged by visual inspection. For each of these batches, the hexagonal modification was confirmed by unit-cell measurements on several crystals. These batches were used to further characterize **1**.

FT-IR spectra of **1** reveal the presence of the typical vibrations of the ligand $(talen^{t\text{-}Bu_2})^{6-}$ in the heptanuclear complexes $\mathbf{[Mn^{III}_6M^c]^{3+}}$.[26–28] Additionally, the symmetric $\nu(C{\equiv}N)$ vibration of the bridging $[Mn^{III}(CN)_6]^{3-}$ unit is detected at 2133 cm^{-1}. The shift of the band to higher energies compared to $K_3[Mn^{III}(CN)_6]$, which exhibits the respective band at 2114 cm^{-1}, is consistent with the symmetric bridging mode of the central hexacyanometallate as found in other $\mathbf{[Mn^{III}_6M^c]^{3+}}$ complexes.[26–28] ESI mass spectra of **1** show signals at mass-to-charge-ratios m/z of 917.0 and 1375.8 with a mass and isotope distribution pattern corresponding to the trication $[\{(talen^{t\text{-}Bu_2})Mn_3\}_2\{Mn(CN)_6\}]^{3+}$ and the dication $[\{(talen^{t\text{-}Bu_2})Mn_3\}_2\{Mn(CN)_6\}]^{2+}$, respectively. The successful formation of $\mathbf{[Mn^{III}_6Mn^{III}]^{3+}}$ is also evident from MALDI-TOF mass spectra of **1**, which exhibit a signal at

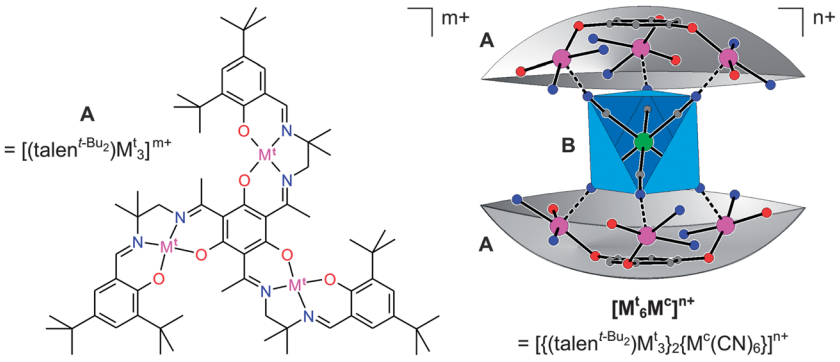

Scheme 1

m/z = 2751.8 corresponding to the monocation $[\{(talen^{t\text{-}Bu_2})Mn_3\}_2\{Mn(CN)_6\}]^+$.

Molecular and crystal structure

1 crystallizes in the space group $R\bar{3}$. The asymmetric unit consists of two independent metal-containing entities, each forming a sixth of a $\mathbf{[Mn^{III}_6Mn^{III}]^{3+}}$ complex (Fig. S1 in the ESI†). The individual molecules are generated by crystallographic S_6 axes. The $\mathbf{[Mn^{III}_6Mn^{III}]^{3+}}$ complex consists of two trinuclear Mn^{III} triplesalen building blocks connected by a central $[Mn^{III}(CN)_6]^{3-}$ unit (Fig. 1). Each terminal Mn^{III} ion is coordinated by the N_2O_2 donor set of a salen-like ligand compartment, with Mn–O and Mn–N distances of 1.88–1.89 Å and 1.97–1.98 Å, respectively. The remaining coordination sites are occupied by a nitrogen atom of the $[Mn^{III}(CN)_6]^{3-}$ unit, with Mn–$N^{C\equiv N}$ distances of 2.19 Å, and by the oxygen atom of a weakly coordinating methanol molecule, with Mn–O^{MeOH} distances of 2.29 and 2.33 Å for the two independent molecules.

The central $[Mn^{III}(CN)_6]^{3-}$ core is slightly compressed along the molecular S_6 axis, as evidenced by C–Mn–C angles within one half of a $\mathbf{[Mn^{III}_6Mn^{III}]^{3+}}$ complex of 90.7 and 91.9°. Within the Mn–C≡N units, the Mn–C bond lengths are 1.98 and 1.99 Å and the C≡N bond distances are 1.15 Å. While the Mn–C≡N units are almost linear (178.6 and 178.9°), the C≡N–Mn connections are bent towards the molecular S_6 axis with angles of 160.0 and 161.7°. Selected interatomic distances and angles of **1** are summarized in Table S1 (ESI†).

In addition to the high molecular symmetry (S_6) of the $\mathbf{[Mn^{III}_6Mn^{III}]^{3+}}$ molecules, the high symmetry of the crystal structure (space group $R\bar{3}$) enforces that the molecular S_6 axes of the $\mathbf{[Mn^{III}_6Mn^{III}]^{3+}}$ complexes are all aligned with the c axis of the unit-cell (Fig. 2). A second positive effect of the high symmetry of the crystal structure is the regular symmetric environment of each individual $\mathbf{[Mn^{III}_6Mn^{III}]^{3+}}$ molecule in the crystal structure (Fig. 2c). The distance between neighboring molecules is best described by the shortest Mn···Mn distance between central Mn^{III} ions that is 15.81 Å. However, the shortest intermolecular Mn···Mn distance of 8.84 Å obviously involves terminal Mn^{III} ions.

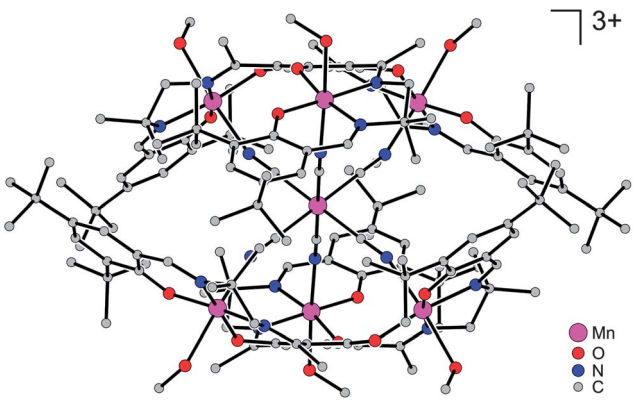

Fig. 1 Molecular structure of $[\{(talen^{t\text{-}Bu_2})(Mn^{III}(MeOH))_3\}_2\{Mn^{III}(CN)_6\}]^{3+}$ in crystals of **1**. Hydrogen atoms are omitted for clarity.

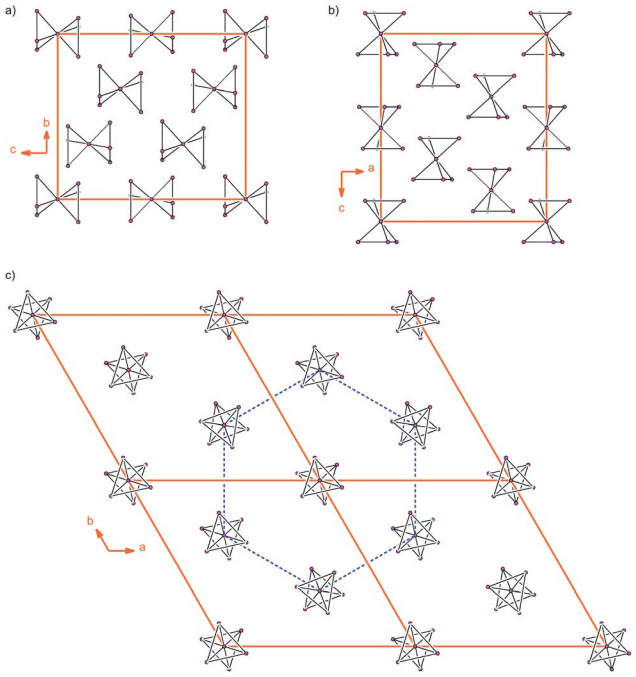

Fig. 2 Sections of the crystal structure of **1** with the viewing direction parallel to (a) the a axis, (b) the b axis, and (c) the c axis of the unit-cell. The $\mathbf{[Mn^{III}_6Mn^{III}]^{3+}}$ molecules are simplified to connected Mn atoms. Note that the molecular S_6 axes of the $\mathbf{[Mn^{III}_6Mn^{III}]^{3+}}$ complexes are all parallel to the c axis. The dashed lines in (c) highlight the hexagonal packing of the molecules.

Magnetic properties

Magnetic measurements on bulk samples. Temperature-dependent magnetic susceptibility measurements (2–290 K, 1 T) on bulk samples of **1** reveal an effective magnetic moment μ_{eff} = 11.84 μ_B at 290 K, which decreases monotonously with decreasing temperature to a minimum of 6.71 μ_B at 2 K (Fig. 3a). The monotonous decrease of μ_{eff} with decreasing temperature indicates dominant antiferromagnetic interactions between the metal ions. It should be noted that the expected coupling scheme consisting of six terminal Mn^{III} h.s. ions ($S_i = 2$) and one central Mn^{III} l.s. ion ($S_i = 1$) would result in a ferrimagnetic coupling scheme, as observed for $\mathbf{[Mn^{III}_6Cr^{III}]^{3+}}$,[26] with an increase of μ_{eff} at lower temperatures.

The M *vs.* B curve at 1.8 K shows a continuous increase of the magnetization with increasing field without exhibiting saturation behavior even at the highest field of 5 T, where the magnetization reaches a value of 14.42 μ_B (Fig. 3b). However, between 1 T and 4 T the increase of M is not strictly linear, but shows a shallow dip at around 2 T. This feature is the onset of a step-like behavior which becomes more pronounced at much lower temperatures (*vide infra*). The isofield lines at 1, 4, and 7 T in the VTVH measurements (Fig. 3c) exhibit a strong nesting behavior, which is indicative of strong magnetic anisotropy,[49] and show a more pronounced saturation behavior with increasing magnetic field, with the magnetization reaching a value of 16.76 μ_B at 2 K/7 T. At low temperatures and zero DC field, **1** exhibits an onset of the out-of-phase component of the AC susceptibility (Fig. 4), demonstrating a slow relaxation of the magnetization indicative

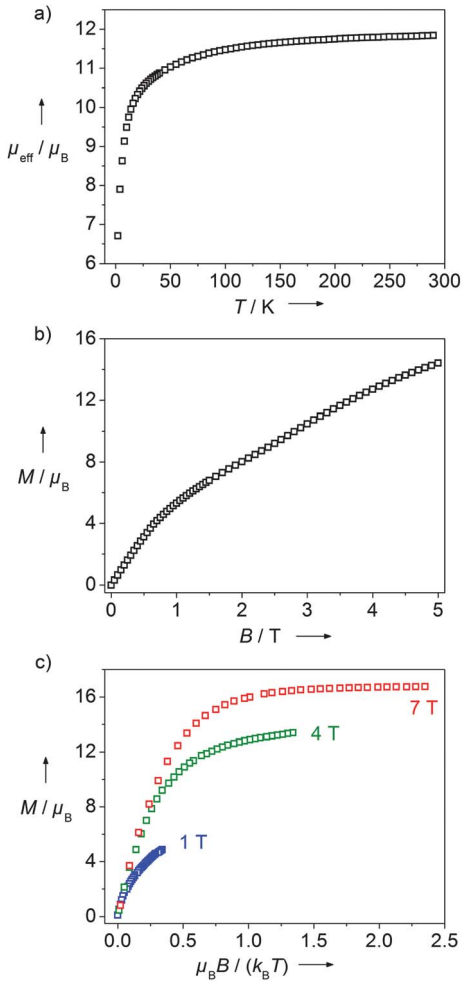

Fig. 3 Magnetic measurements on bulk samples of **1**. (a) Temperature-dependence of μ_{eff} at 1 T. (b) Field-dependence of the magnetization at 1.8 K. (c) VTVH magnetization measurements at 1 T (blue), 4 T (green), and 7 T (red).

of single-molecule magnet behavior. However, the large ratio $\chi'_M/\chi''_M = 63$ at 1.8 K/1488 Hz, as well as the absence of both a frequency dependence and a decrease in the magnitude of χ'_M within the accessible temperature range, hint at a very low effective energy barrier for magnetization reversal U^{eff}.

***Ab initio* calculations for the central Mn^{III} l.s.** The central Mn^{III} ion is in the low-spin configuration (Fig. 5a). In O_h symmetry, this results in a $^3T_{1g}$ ground state. In the absence of a trigonal splitting Δ_1 of the $^3T_{1g}$ term, the orbital momentum of the complex is not quenched and corresponds to an effective $\tilde{L} = 1$.[50] This couples to the total spin $S = 1$ by the effective spin-orbit interaction $\lambda\tilde{\mathbf{L}}\cdot\mathbf{S}$, where $\lambda = \zeta/2S$ and $\zeta = 360$ cm^{-1} is the spin-orbit coupling constant for the Mn^{III} ion.[50] As the t_{2g} shell is more than half-filled (see Fig. 5a), in the case of conventional spin-orbit coupling one should have taken the expression for λ with negative sign.[50] However, the matrix elements of orbital momentum in eigenstates of effective $\tilde{L} = 1$ have opposite sign with respect to similar matrix elements calculated in the eigenstates of a true momentum $L = 1$,[50] therefore the sign of λ remains positive. The states resulting from this coupling

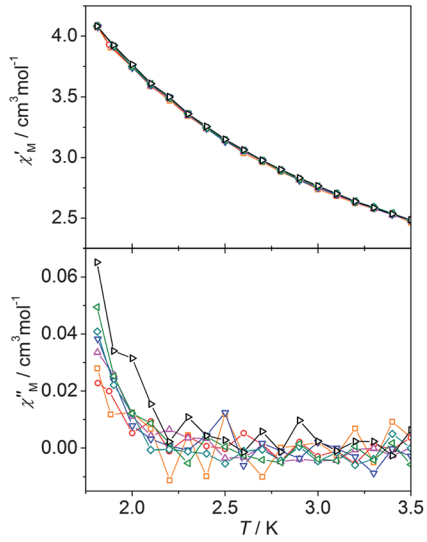

Fig. 4 Plots of the in-phase (χ'_M) and the out-of-phase (χ''_M) component of the AC susceptibility *versus* the temperature for **1** at zero DC field, with an AC field of 3 Oe oscillating at a frequency of 660 (orange), 801 (red), 938 (magenta), 1078 (blue), 1218 (cyan), 1359 (green), and 1488 Hz (black). Solid lines are a guide to the eye.

correspond to conserved total effective momentum ($\tilde{\mathbf{J}} = \tilde{\mathbf{L}} + \mathbf{S}$) with $\tilde{J} = 0, 1, 2$ in full analogy to the summation of true orbital and spin momenta in free atoms. Accordingly, the spectrum consists of three multiplets corresponding to definite $\tilde{J}$, each being $(2\tilde{J} + 1)$-fold degenerate. The separation between neighboring $\tilde{J} - 1$ and $\tilde{J}$ multiplets is described by the Lande's rule,[50] $\Delta E = \lambda\tilde{J}$. Given $\lambda > 0$, the ground multiplet corresponds to $\tilde{J} = 0$, *i.e.* is non-magnetic, while the first excited multiplet is $\tilde{J} = 1$ with the energy $\Delta E = \lambda = \zeta/2 = 180$ cm^{-1}.[37,41] The temperature-dependence of μ_{eff} of $[(Ph_3P)_2N]_3[Mn^{III}(CN)_6]$ exhibits a

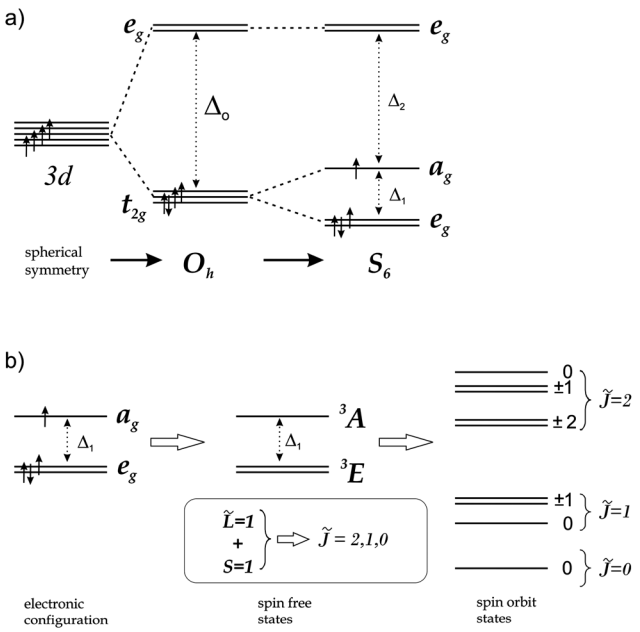

Fig. 5 (a) Splitting of the five 3d orbitals upon symmetry lowering, and (b) lowest spin-free states and the resulting spin-orbit states, for Mn^{III} in an S_6 symmetry environment.

continuous decrease of μ_{eff} from 3.98 μ_B at 300 K to 3.57 μ_B at 100 K and then to 0.79 μ_B at 2 K. These data were analyzed including first-order spin-orbit coupling providing an estimate of $\lambda = 140$ cm^{-1}.[38]

The symmetry of the central Mn^{III} ion in $[Mn^{III}_6Mn^{III}]^{3+}$ is reduced from O_h to S_6 by a compression of the local octahedron along the C_3 axis and by the non-linear Mn^{III}(central)–C≡N–Mn^{III}(terminal) units that are bent towards the S_6 axis enforced by the triplesalen ligand. This leads to a splitting of the t_{2g} orbitals into a_g and e_g with the e_g orbitals being lowest in energy (Fig. 5a). The $e_g^3a_g^1$ electron configuration results in a spin-free ^3E ground state (Fig. 5b).

The presence of this trigonal (axial) crystal field Δ_1 splits the excited $\tilde{J}$ multiplets into axial doublets, with opposite projections of $\tilde{\mathbf{J}}$ on the trigonal axis of the complex, and singlets (Fig. 5b). The split multiplets are characterized by definite $M_{\tilde{J}}$, strictly speaking, in the presence of an S_6 axis. In the case of a C_3 axis there will be a small mixing of $M_{\tilde{J}} = \pm1$ and $M_{\tilde{J}} = \pm2$ doublets belonging to the $\tilde{J} = 2$ multiplet.

In order to gain more quantitative insight into the electronic structure and magnetic properties of this ion under the perturbed structure in $[Mn^{III}_6Mn^{III}]^{3+}$, we performed *ab initio* calculations (CASSCF/CASPT2) taking into account spin-orbit coupling for the central Mn^{III} l.s. in four structural approximations differing in the way the surrounding six Mn^{III} ions were treated (see computational details in the *Experimental section*). Common to all approximations is that the central Mn^{III} ion is the only open-shell atom so that its electronic and magnetic properties can easily be extracted from the calculations. The results of these calculations for the four approximations are summarized in Tables 1–5.

Depending on the approximation and the inclusion of second-order corrections to the energy, the three components of the $\tilde{J} = 1$ multiplet are ≈ 130–190 cm^{-1} and the five components of the $\tilde{J} = 2$ multiplet are ≈ 400–600 cm^{-1} above the $\tilde{J} = 0$ ground state. This implies that the central Mn^{III} ion is non-magnetic at low temperatures, while magnetic substates become populated at higher temperatures. The three lowest $\tilde{J} = 1$ and $\tilde{J} = 2$ multiplets exhibit Ising behavior (Table 5) with the lowest $\tilde{J} = 1$ multiplet having only a small g_z component.

As the quantum chemistry calculations show, the groups of levels belonging to given $\tilde{J}$ multiplets are well separated. Therefore the energy gaps between the ground singlet state and the first excited multiplets is mostly due to the strong (first-order) spin-orbit coupling effect, which is the result of unquenched orbital momentum in the complex, and not to the trigonal component of the crystal field.

The destructive manifestation of unquenched orbital momentum is entirely due to the positive sign of the effective spin-orbit coupling constant λ which determines the order of $\tilde{J}$ multiplets on Mn^{III}. Note that contrary to the zero-field splitting parameter D, which is a second-order effect of spin-orbit coupling,[50] the sign of λ does not depend on the crystal field. In particular, λ remains positive for both elongation and compression of the octahedral environment of Mn^{III}. The only factor influencing the sign of λ (and the order of multiplet states in Fig. 5b) is the population of the t_{2g} shell of the metal ion (Fig. 5a), which should be less than half-filled in order to have $\lambda < 0$. This would be the case, for instance, for d^2 transition metal ions in a similar environment, like for hexacyanometallates of V^{III}, Nb^{III}, and Ta^{III}. For these metal ions the order of the multiplet states in Fig. 5b will be reversed resulting in the stabilization of the $M_{\tilde{J}} = \pm2$ doublet (for unchanged sign of Δ_1), thus opening the way for producing very strong SMMs with

Table 1 CASSCF/CASPT2 energies (cm^{-1}) of the spin-free states (left) and of the resulting lowest spin-orbit states (right) for approximation A

Spin Multiplicity	Spin-Free Energies		Spin-Orbit Energies	
	CASSCF	CASPT2	CASSCF	CASPT2
	5383.623	15403.028	0.000	0.000
	5383.623	15423.902	139.438	155.220
5	34258.676	48643.486	170.826	184.793
	34258.676	48699.169	170.826	187.564
	34416.935	48749.016	412.343	431.759
	0.000	0.000	412.343	432.482
	0.000	4.024	483.568	512.382
3	104.076	112.998	483.568	512.901
	24270.077	27435.337	503.940	530.012
	24270.077	27484.078	5680.791	5472.004
	…	…	5683.444	6043.700
	11186.849	5156.235	5691.016	6585.084
	11445.670	5736.077	5691.016	7363.883
1	11445.670	6278.314	5699.442	7823.241
	12837.368	7058.728	5699.442	15704.761
	12837.368	7518.795	5703.935	15704.858
	22891.349	15936.159	5713.406	15708.890
	…	…	5713.406	15710.035
			5715.300	15711.504
			11477.466	15731.563
			11736.085	15732.193
			11736.085	15734.704
			13127.538	15736.841
			13127.538	15737.114
			23175.250	16248.641
			24558.234	27731.553
			24565.350	27735.741
			…	…

Table 2 CASSCF energies (cm^{-1}) of the spin-free states (left) and of the resulting lowest spin-orbit states (right) for approximation B

Spin Multiplicity	Spin-Free Energies	Spin-Orbit Energies
	CASSCF	CASSCF
	4942.841	0.000
	4942.899	150.926
5	33479.846	167.523
	33479.923	167.525
	33712.759	423.011
	0.000	423.011
	0.003	471.793
3	66.577	471.794
	23831.909	489.496
	23831.909	5252.090
	…	5254.869
	11196.048	5263.631
	11452.462	5263.644
1	11452.462	5273.138
	12849.641	5273.174
	12849.643	5278.157
	22818.510	5288.830
	…	5288.838
		5290.581
		11499.130
		11755.316
		11755.317
		13152.316
		13152.318
		23112.542
		24131.312
		…

Table 3 CASSCF/CASPT2 energies (cm^{-1}) of the spin-free states (left) and of the resulting lowest spin-orbit states (right) for approximation C

Spin Multiplicity	Spin-Free Energies		Spin-Orbit Energies	
	CASSCF	CASPT2	CASSCF	CASPT2
	4921.570	14981.893	0.000	0.000
	4921.612	15005.710	119.115	135.507
5	33455.920	47844.383	177.331	190.366
	33455.935	47854.369	177.331	197.625
	33526.900	47934.249	395.636	415.856
	0.000	0.000	395.636	415.894
	0.001	8.833	531.138	561.804
3	196.157	209.812	531.138	563.527
	23778.281	26863.924	556.698	584.967
	23778.281	26924.641	5203.240	5105.288
	…	…	5207.066	5951.642
	11186.565	4807.679	5213.779	6650.978
	11499.874	5664.350	5213.793	7332.451
1	11499.875	6365.228	5222.271	7685.900
	12882.497	7047.498	5222.291	15265.003
	12882.498	7401.686	5227.033	15265.192
	22818.369	15750.189	5235.896	15268.105
	…	…	5235.904	15269.593
			5239.098	15270.481
			11459.972	15292.936
			11772.959	15293.232
			11772.959	15295.835
			13155.420	15297.110
			13155.421	15297.550
			23082.470	16042.626
			24050.879	27140.439
			24056.452	27144.685
			…	…

energy barriers for spin reversal being directly influenced by the strength of exchange interactions with surrounding metal ions, as proposed earlier.[51] The synthesis of such compounds on the basis of highly symmetric polynuclear complexes discussed here represents a challenging task for future investigations.

Table 4 CASSCF energies (cm^{-1}) of the spin-free states (left) and of the resulting lowest spin-orbit states (right) for approximation D

Spin Multiplicity	Spin-Free Energies	Spin-Orbit Energies
	CASSCF	CASSCF
	5003.608	0.000
	5003.887	129.311
5	33598.079	174.802
	33598.334	174.928
	33719.548	404.973
	0.000	404.975
	0.177	504.097
3	146.801	504.145
	23877.180	527.512
	23877.342	5294.389
	…	5297.869
	11195.188	5304.893
	11475.026	5304.984
1	11475.111	5313.406
	12862.021	5313.540
	12862.181	5318.168
	…	5327.169
		5327.221
		5330.073
		11478.034
		11757.606
		11757.690
		13144.422
		13144.582
		…

The results of these *ab initio* calculations explain the unexpected μ_{eff} *vs.* T behavior of $[Mn^{III}_6Mn^{III}]^{3+}$ (*vide supra*). As the central Mn^{III} is essentially diamagnetic, the magnetism of $[Mn^{III}_6Mn^{III}]^{3+}$ arises only from the terminal Mn^{III} ions. This coupling scheme coincides with that of $[Mn^{III}_6Co^{III}]^{3+}$ (central diamagnetic Co^{III} l.s.), which also exhibits a continuous decrease of μ_{eff} with decreasing temperature.[28]

Magnetic measurements on single-crystals. To prove the basic property of an SMM – namely an open hysteresis of the magnetization below a certain blocking temperature T_B – we have performed low-temperature magnetization measurements on single-crystals of **1** employing a home-made micro-Hall probe magnetometer. The low-field section is depicted in Fig. 6a. It reveals an open hysteresis between fields of ±1.5 T with a coercive field of $\mu_0 H_c = 50$ mT, clearly showing the SMM nature of **1**. After an intermediate saturation between 0.6 T and 1.0 T, the magnetization increases further at higher fields. This is clear evidence that an excited state starts to become partially populated already at these rather low fields. To investigate the behavior of the magnetization at high fields, measurements up to 12 T were carried out (Fig. 6b). Surprisingly, it becomes evident that not only the spin ground state shows a hysteretic behavior, but also the excited state. Thus, $[Mn^{III}_6Mn^{III}]^{3+}$ is a true single-molecule magnet not only in the low-field ground state, but also in an excited state becoming ground state at high fields.

The ratio between the magnetization at fields of about 1.8 T and the magnetization at 10 T (dotted lines in Fig. 6b) has a value of $M_{s_2}/M_{s_1} = 3.07$. A value of almost 3 fits perfectly in the context of six exchange coupled $S_{Mn} = 2$ spins with a ground state $S_{t,1} = 8/2$ and an excited state $S_{t,2} = 24/2$ (insets in Fig. 6b). Hence, this experimental result nicely confirms the diamagnetic nature of the central Mn^{III} l.s. at low temperatures as evident from the *ab initio* calculations (*vide supra*).

The hysteresis of both openings closes at a blocking temperature of about $T_B \approx 2.0$ K. A plot depicting the angular dependence of the magnetization up to 10 T is provided in Fig. 7. This figure nicely illustrates that the transition from the ground state to the excited state is shifted to higher fields for larger angles between the *c* axis of the unit-cell and the field direction, and that the two hysteretic parts almost converge at certain angles. Thus, the energy needed for the transition from $S_{t,1} = 8/2$ to $S_{t,2} = 24/2$ appears to be highest for angles around 30°.

Quantum spin-Hamiltonian simulations. In order to gain some quantitative insight not only into magnitudes and ratios of the exchange couplings J_{ij} and zero-field splittings D_i, but also into the remarkable double hysteresis, we have performed a full-matrix diagonalization of the appropriate spin-Hamiltonian including isotropic HDvV exchange, zero-field splitting, and Zeeman interaction (see computational details in the *Experimental section*). In accordance with the results of the *ab initio* calculations (*vide supra*), we have evaluated the magnetic properties of $[Mn^{III}_6Mn^{III}]^{3+}$ in terms of a spin system consisting of only the six terminal Mn^{III} h.s. ions ($S_i = 2$) and neglecting the central Mn^{III} l.s. ion (Fig. 8). We have incorporated the zero-field splitting for the terminal Mn^{III} ions including the relative orientations of the individual **D**-tensors by the angle ϑ of the Jahn–Teller axes with the molecular axis. Considering that in

Table 5 g_z components of the g tensor of three Ising doublets. The g_x and g_y components are zero. The magnetic moment corresponding to g_z is oriented along the S_6 symmetry axis of the complex

	A		B	C		D
Origin	CASSCF	CASPT2	CASSCF	CASSCF	CASPT2	CASSCF
$\tilde{J} = 1$	0.057	0.122	0.401	0.598	0.546	0.275
$\tilde{J} = 2$	2.028	2.116	2.036	2.023	2.108	2.026
$\tilde{J} = 2$	1.969	2.012	1.634	2.622	2.640	2.302

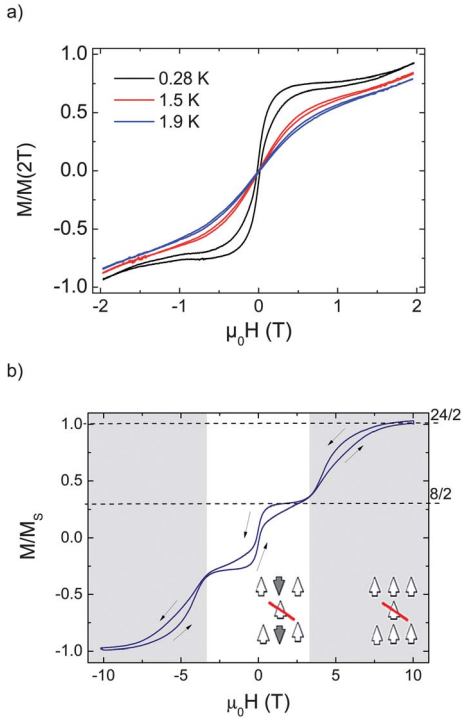

Fig. 6 (a) Magnetization curves of a single-crystal of **1** at three different temperatures. The sample is oriented such that the magnetic field is parallel to the c axis of the unit-cell. (b) Magnetization *vs* field up to 10 T at 0.32 K. This measurement reveals hysteresis of the ground state (white area) and of an excited state (grey areas). The broken lines indicate the spin state at the position of a local saturation. The insets illustrate the corresponding spin orientation. The angle between magnetic field and the c axis of the unit-cell is $\approx 35°$ in this measurement.

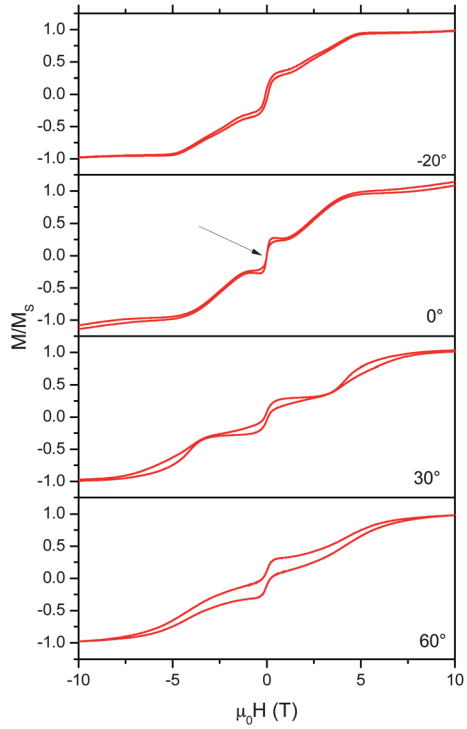

Fig. 7 Angular dependence of the magnetization at low temperatures. The data has been recorded at a temperature of 0.3 K and a sweep rate of 12.5 mT s^{-1}. The arrow in the second plot indicates the smallest coercive field.

$[Mn^{III}_6M^c]^{n+}$ the exchange interaction of the Mn^{III} ions with paramagnetic central ions such as Cr^{III} can reach values up to 5 cm^{-1},[26] it seems reasonable to assume that there is a remaining interaction through the central singlet in $[Mn^{III}_6Mn^{III}]^{3+}$. This has already been established for $[Mn^{III}_6Co^{III}]^{3+}$, which possesses a central diamagnetic Co^{III} ion through which the Mn^{III} ions of different trinuclear triplesalen subunits exhibit a weak ferromagnetic coupling of $+(0.05 \pm 0.02)$ cm^{-1}.[28] In order to evaluate the magnetic properties of $[Mn^{III}_6Mn^{III}]^{3+}$, we therefore used a coupling scheme incorporating not only an exchange interaction between the Mn^{III} ions within a trinuclear triplesalen subunit ($J^{(1)}_{Mn-Mn}$), but also across the central Mn^{III} between Mn^{III} ions belonging to different trinuclear triplesalen subunits ($J^{(2)}_{Mn-Mn}$). Taking into account the S_6 symmetry, we incorporated two different couplings *via* the central Mn^{III}, namely that of a Mn^{III} ion in one trinuclear building block with the Mn^{III} ions in *cis* position of the other building block ($J^{(2,cis)}_{Mn-Mn}$), and the respective *trans* coupling ($J^{(2,trans)}_{Mn-Mn}$).

The spin-Hamiltonian parameters of $[Mn^{III}_6Mn^{III}]^{3+}$ have been determined with the help of a fitting routine. Two parameter sets (A: $J^{(1)}_{Mn-Mn} = -0.345$ cm^{-1}, $J^{(2,cis)}_{Mn-Mn} = -0.025$ cm^{-1}, $J^{(2,trans)}_{Mn-Mn} = -0.015$ cm^{-1}, $D_{Mn} = -3.05$ cm^{-1}, $\vartheta = 37.5°$; B: $J^{(1)}_{Mn-Mn} = -0.43$ cm^{-1}, $J^{(2,cis)}_{Mn-Mn} = +0.07$ cm^{-1}, $J^{(2,trans)}_{Mn-Mn} = +0.04$ cm^{-1}, $D_{Mn} = -3.20$ cm^{-1}, $\vartheta = 37.5°$) yield equally good χ^2 deviations for the VTVH data of **1**, where all data have been considered with equal weight. From all the simulations that we did perform, we estimate the error ± 0.005 cm^{-1} for all exchange couplings and ± 0.05 cm^{-1} for D_{Mn} (some of these simulations are provided in Fig. 9–11). Since the low-temperature data are more prominent in the VTVH measurements, these parameterizations provide an excellent representation of the low-energy Hamiltonian. As illustrated in Fig. 9 (parameter set A) and Fig. 10 (parameter set B), variations of the parameters of the order of $+/-0.05$ cm^{-1} result in mild deviations from the best fits, which provides an estimate of the accuracy and

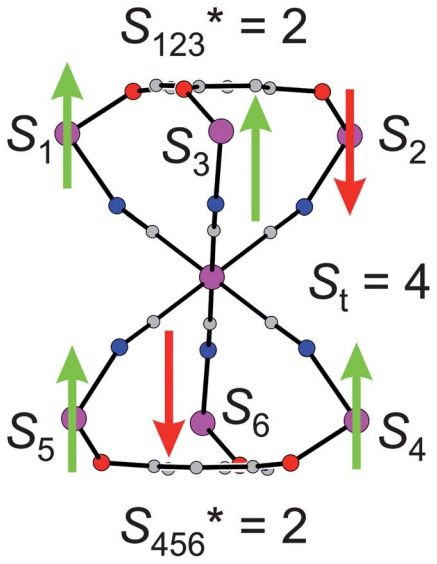

Fig. 8 Coupling scheme illustrating the $S_t = 4$ spin ground state of $[Mn^{III}_6Mn^{III}]^{3+}$.

the width of the minima of the χ^2 function in the parameter space. Simulations assuming no interaction *via* the central Mn^{III} l.s. ($J^{(2,cis)}_{Mn-Mn} = J^{(2,trans)}_{Mn-Mn} = 0$ cm^{-1}) also reproduce the experimental data qualitatively (Fig. 11), but yield larger χ^2 deviations.

The temperature-dependence of μ_{eff} for **1** is well approximated by parameter sets A and B at low and high temperatures (Fig. 12a). At intermediate temperatures of 25–75 K, deviations are visible. We conjecture that these deviations arise from the thermal population of the excited magnetic levels of the central Mn^{III} l.s.

The shallow dip in the *M vs. B* curve of **1** at 1.8 K is approximately reproduced by parameter set B, while no such feature appears in the simulation with parameter set A (Fig. 12b). This indicates that the coupling of the trinuclear triplesalen subunits

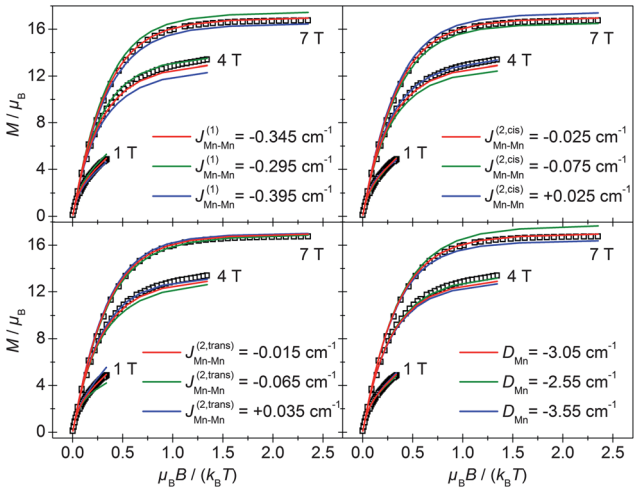

Fig. 9 Simulations of the VTVH data of **1** performed by a full-matrix diagonalization of the complete spin-Hamiltonian using parameter set A (red lines) except for the variation of $J^{(1)}_{Mn-Mn}$ (top left panel), $J^{(2,cis)}_{Mn-Mn}$ (top right panel), $J^{(2,trans)}_{Mn-Mn}$ (bottom left panel) of the order of +/−0.05 cm^{-1}, or D_{Mn} (bottom right panel) of the order of +/−0.5 cm^{-1}.

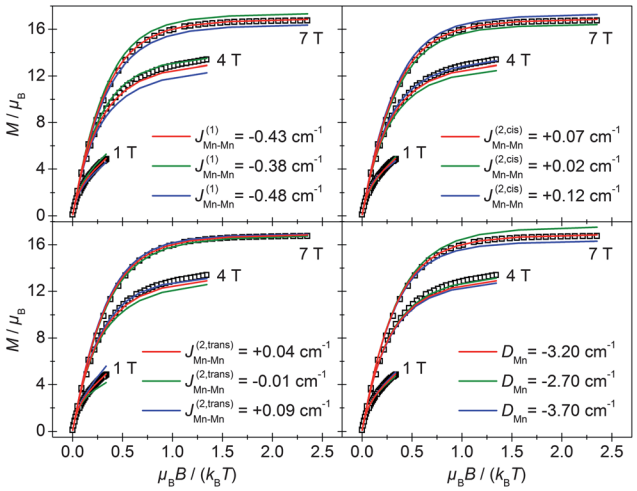

Fig. 10 Simulations of the VTVH data of **1** performed by a full-matrix diagonalization of the complete spin-Hamiltonian using parameter set B (red lines) except for the variation of $J^{(1)}_{Mn-Mn}$ (top left panel), $J^{(2,cis)}_{Mn-Mn}$ (top right panel), $J^{(2,trans)}_{Mn-Mn}$ (bottom left panel) of the order of +/−0.05 cm^{-1}, or D_{Mn} (bottom right panel) of the order of +/−0.5 cm^{-1}.

via the central Mn^{III} l.s. is more likely slightly ferromagnetic (parameter set B) than antiferromagnetic (parameter set A).

In the limit of strong exchange ($J \gg D$), these coupling constants can explain the spin ground state $S_{t,1} = 4$ and field-induced ground state $S_{t,2} = 12$. The antiferromagnetic exchange interaction in the trinuclear Mn^{III}_3 triplesalen subunits ($J^{(1)}_{Mn-Mn}$) results in intermediate $S_{123}* = S_{456}* = 2$ spins (Fig. 8), which are coupled to an $S_{t,1} = 4$ spin ground state of the whole molecule by the weak ferromagnetic exchange interaction across the central diamagnetic Mn^{III} ($J^{(2)}_{Mn-Mn}$). The Zeeman energy at $\approx$ 3.4 T is sufficient to overcome the antiferromagnetic exchange and the anisotropy energy in the trinuclear subunits so that all spins are aligned parallel resulting in the new $S_{t,2} = 12$ spin ground state. However, the obtained parameters clearly establish that $[Mn^{III}_6Mn^{III}]^{3+}$ is in the limit of weak exchange ($J \ll D$).

In order to discuss the consequences on the magnetization curve of $[Mn^{III}_6Mn^{III}]^{3+}$, it is instructive to first look at a triangular subunit as given by one of the caps. As these units are magnetically only weakly coupled *via* the central Mn^{III} l.s., the magnetism of $[Mn^{III}_6Mn^{III}]^{3+}$ is to a large extent dominated by their properties.

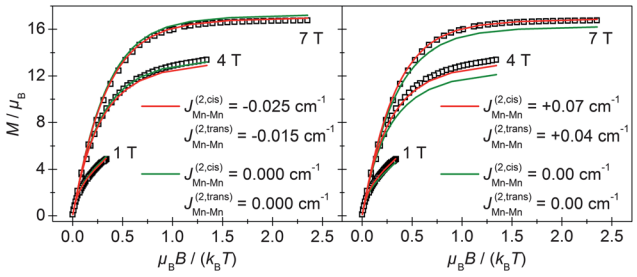

Fig. 11 Simulations of the VTVH data of **1** performed by a full-matrix diagonalization of the complete spin-Hamiltonian using parameter sets A (left panel, red lines) and B (right panel, red lines) and a variation of each set assuming no interaction *via* the central Mn^{III} l.s. ($J^{(2,cis)}_{Mn-Mn} = J^{(2,trans)}_{Mn-Mn} = 0$ cm^{-1}, green lines).

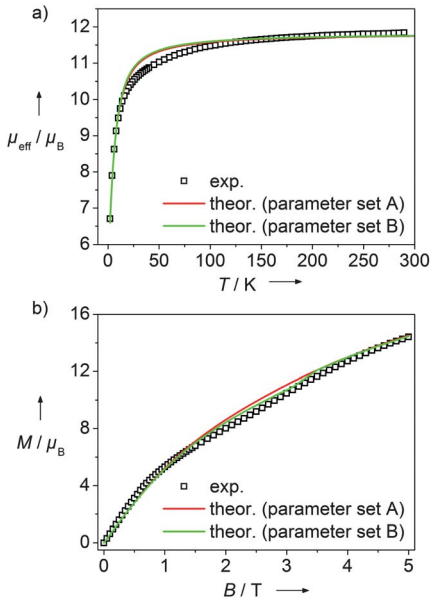

Fig. 12 Simulations of (a) the μ_{eff} *vs.* T data at 1 T and (b) the M *vs.* B data at 1.8 K of **1** performed by a full-matrix diagonalization of the complete spin-Hamiltonian using parameter sets A (red) and B (green).

We describe the triangles as three antiferromagnetically coupled $S_i = 2$ spins with local easy axes.[52] The antiferromagnetic coupling is kept fixed and only the easy axes varied in strength and direction. The whole system is kept in C_3 symmetry.

The left column of Fig. 13 shows how the energy spectrum changes for collinear easy axes by increasing the local D_i values. The x-axis represents the magnetization of the various eigenstates. For the collinear scenario, M_{S_t} is a good quantum number since $[\hat{H}, S_t^z] = 0$. Therefore, the magnetization of an eigenstate equals $g \cdot M_{S_t}$. The antiferromagnetic coupling of three isotropic $S_i = 2$ spins results in an $S_t = 0$ ground state with $S_t = 1, 2, \ldots, 6$ at higher energies (Fig. 13, top left panel). For small absolute values of D_i compared to the absolute value of the exchange, the ground state remains a singlet as for $D_i = 0$ (Fig. 13, middle left panel). For large enough D_i, *i.e.* in the weak exchange limit, a low-energy barrier develops for a quantization axis along the C_3 axis (Fig. 13, bottom left panel).

This situation changes completely for a configuration as in $[Mn^{III}_6Mn^{III}]^{3+}$ where the local easy axes have a common angle of 37.5° to the C_3 axis. In this case, M_{S_t} is no longer a good quantum number, and the magnetization of each eigenstate corresponds to the expectation value for a tiny magnetic field $B_z = 0.001$ T along the C_3 axis. If one now looks at the spectrum for a quantization axis along the C_3 axis (realized by the tiny magnetic field), one notices (i) the removal of degeneracies compared to the collinear arrangement, and (ii) that the ground state remains diamagnetic and no barrier develops (Fig. 13, right column), not even for a $D_i/J_1 = 2$ ratio where a barrier is observed for the collinear scenario (Fig. 13, bottom panels). The reason is that the contributions of the individual easy axes almost cancel for the combined system.

Fig. 14 shows corresponding energy spectra for the whole $[Mn^{III}_6Mn^{III}]^{3+}$ complex calculated with parameter set B. Since M_{S_t} is again not a good quantum number, the magnetization of each eigenstate as represented on the x-axis corresponds to the expectation value for a small magnetic field along the C_3 axis ($B_z = 0.01$ T; Fig. 14, left panels) and along $\vartheta = 40°$ ($B_{40} = 0.01$ T; Fig. 14, right panels), *i.e.* almost along the direction of two local D_i tensors. It is evident from Fig. 14 that (i) a low-energy barrier develops for both field directions, and (ii) at low energies the spectrum for the magnetic field along $\vartheta = 40°$ exhibits eigenstates with larger magnetic moments. This low-energy barrier is the origin of the hysteresis shown in Fig. 6a and of the slight onset of the out-of-phase component of the AC susceptibility in Fig. 4.

However, the complete M *vs.* B data obtained from measurements on single-crystals of **1** at 0.32 K (*vide supra*) is well reproduced in terms of a field-induced change of the spin ground state with parameter set B (Fig. 15). Fig. 16 (right panel) shows the corresponding energy spectrum. For the magnetic field applied along $\vartheta = 40°$, there is a crossing at $\approx$ 3.4 T between eigenstates exhibiting a magnetization in the 9…10 μ_B range with eigenstates having a magnetization of 15…16 μ_B. In contrast, if the magnetic field is applied along the C_3 axis (Fig. 16, left panel), a similar crossing occurs at a smaller field of $\approx$ 2.0 T which involves eigenstates with $M = 6\ldots7\ \mu_B$ and $M = 17\ldots18\ \mu_B$. Thus, the experimentally observed angle-dependence of the hysteresis curves is also reproduced by the quantum-mechanical spin-Hamiltonian simulations.

Classical spin dynamics simulations. We have performed classical spin dynamics simulations using the classical counterpart of the quantum spin-Hamiltonian (see computational details in the *Experimental section*) in order to investigate the field-dependent classical ground state and low-temperature properties, in particular to study the role of the exchange couplings and anisotropies for certain temperatures and external magnetic fields.

Fig. 17 shows the classical ground state configuration of $[Mn^{III}_6Mn^{III}]^{3+}$ as obtained by spin dynamics simulations with parameter set B at $T = 0$ K and $B = 0$ T. This state is one realization of a set of symmetry-related degenerate ground states. The local anisotropy axes of the terminal Mn^{III} ions are depicted as yellow sticks. According to the model parameters, the strong easy-axis anisotropy dominates the orientation of the manganese spins in an up-up-down fashion in both trinuclear subunits. Because of the rather weak exchange interactions in the system, only a very small canting with respect to the anisotropy axes is visible.

This situation changes when an external field is applied. Fig. 18 exhibits simulational results for an external field of 8 T applied in two different directions, namely exactly along the molecular S_6 axis (Fig. 18a) and oriented at 40° to the molecular S_6 axis (Fig. 18b). Compared to the 0 T ground state one finds two manganese spins being flipped, so that the up-up-down configurations are replaced by up-up-up configurations with respect to the field direction. However, the field strength at which the spins flip as well as the size of the magnetization jump are different for the two cases. In the situation where the field is almost aligned to two of the six anisotropy axes of the terminal Mn^{III} ions, the spin flip occurs at a field value of 7.5 T compared to 5 T in the case where the field is aligned to the molecular S_6 axis. This is due to the fact that it costs much more energy to flip a spin which is fully

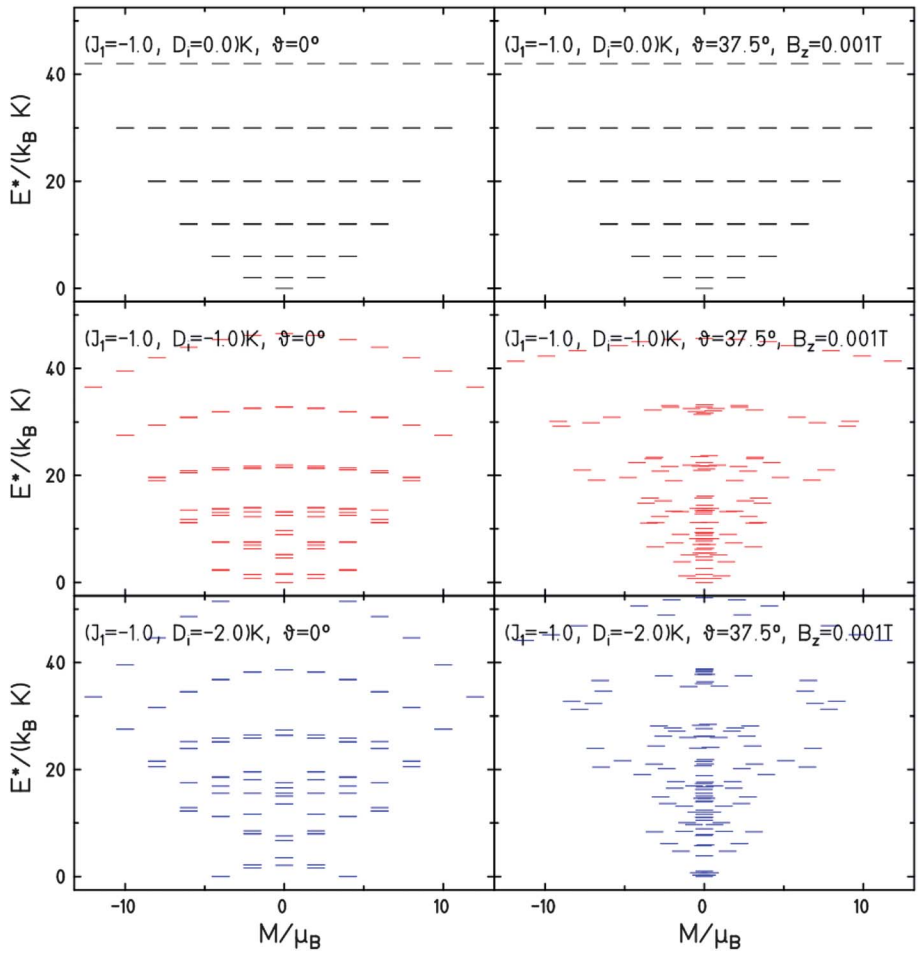

Fig. 13 Energy spectra of a triangular spin system with antiferromagnetic exchange and local easy axes. The *x*-axis represents the magnetization of the various eigenstates. The left column shows the spectra for collinear easy axes, the right column for easy axes with a common angle of 37.5° to the C_3 axis.

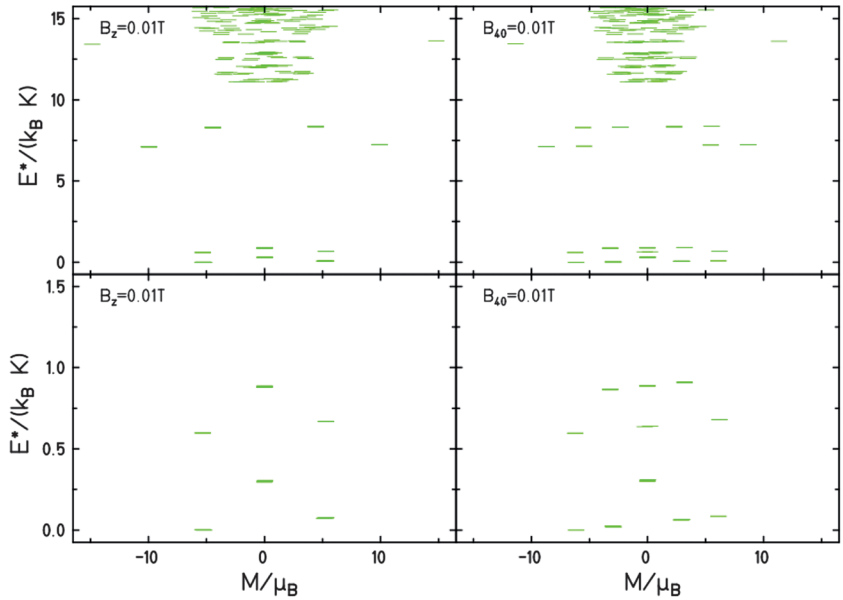

Fig. 14 Energy spectra of $[Mn^{III}_6Mn^{III}]^{3+}$ as a function of the magnetization of each eigenstate (only low-lying levels are shown). The spectra were calculated with parameter set B for a small magnetic field along the C_3 axis ($B_z = 0.01$ T, left panels) and along $\vartheta = 40°$ ($B_{40} = 0.01$ T, right panels). The bottom panels show the lowest energy levels only.

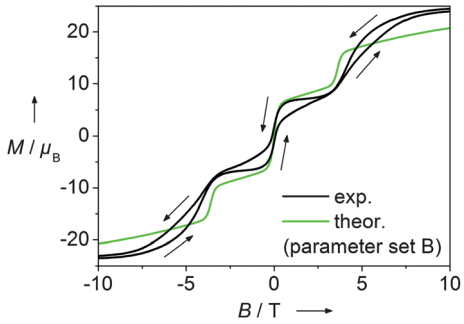

Fig. 15 Comparison of the experimental data obtained from low-temperature high-field micro-Hall-bar measurements on single-crystals of **1** at an angle of ≈ 35° between magnetic field and *c* axis of the unit-cell, with the theoretical curve representing a simulation of the experimental data performed by a full-matrix diagonalization of the complete spin-Hamiltonian using parameter set B with the magnetic field applied along $\vartheta = 40°$.

aligned antiparallel to its local easy-axis compared to one which is canted. Also, the total change of the magnetization according to the spin flips is twice as high in the case of the 40° canted field direction. This is because after the spin flips these spins are fully aligned parallel to their anisotropy axis and to the field direction. In the case of the field applied in the direction of the molecular S_6 axis a canting of the flipped spins remains due to the misalignment of the external field direction and the anisotropy axes. Note that even after all spins are flipped in the field direction the system is still not fully saturated. This is due to the fact that although the Zeeman energy is much larger than the exchange interactions between all spins, the anisotropy energy is still dominant and prevents the spins from full alignment with the external field. In the hysteresis curve this shows up as a slow increase of the magnetization with increasing field after the spin flip. Note that the spin flip fields of our simulations are slightly larger than the experimentally determined fields at which the magnetization jumps occur (see Fig. 15). This is due to the fact that our simulations are carried out at $T = 0$ K. At finite temperatures thermal fluctuations enhance the probability of a spin flip even in lower magnetic fields. In order to visualize the spin-state switching we have prepared movies of our field-dependent classical spin dynamics studies, which can be found in the ESI.† We have also performed finite temperature classical Monte Carlo and spin dynamics simulations which qualitatively

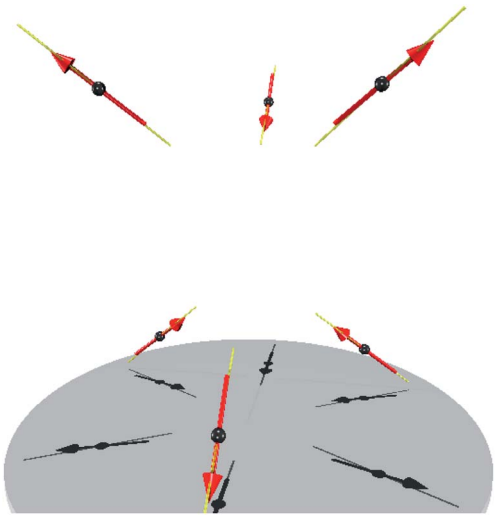

Fig. 17 Classical ground state of $[Mn^{III}_6Mn^{III}]^{3+}$ as obtained by spin dynamics simulations with parameter set B at $T = 0$ K and $B = 0$ T. Yellow bars represent the local anisotropy axes, red arrows the local spin vectors.

show the same results as our exact quantum calculations. We therefore conclude that the steps in the hysteresis are due to the spin-state switching caused by the strong axial anisotropies in both trinuclear units.

Experimental

Preparation of compounds

$H_6talen^{t\text{-}Bu_2}$ { = 2,4,6-tris{1-[2-(3,5-di-*tert*-butylsalicylaldimino)-2-methylpropylimino]-ethyl}-1,3,5-trihydroxybenzene} was synthesized as described previously.[25,53]

$[\{(talen^{t\text{-}Bu_2})(Mn^{III}(MeOH))_3\}_2\{Mn^{III}(CN)_6\}](lac)_3 \cdot 10.5MeOH$ (1). A suspension of $H_6talen^{t\text{-}Bu_2}$ (222 mg, 0.200 mmol) and $Mn(OAc)_2 \cdot 4H_2O$ (135 mg, 0.551 mmol) in methanol (80 mL) was heated at reflux for two hours. The resulting brown solution was cooled to room temperature, purged with air for 30 minutes and heated at reflux for additional two hours. After cooling to room temperature the reaction solution was treated with a solution of $K_3[Mn(CN)_6]$ (32 mg, 0.097 mmol) in water (2 mL). The reaction mixture was stirred at room temperature for 60 minutes and

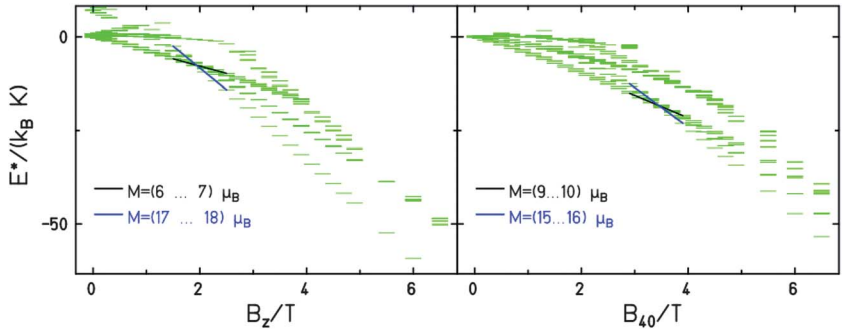

Fig. 16 Energy spectra of $[Mn^{III}_6Mn^{III}]^{3+}$ as a function of the magnetic field applied along the C_3 axis (B_z, left panel) and along $\vartheta = 40°$ (B_{40}, right panel). The spectra were calculated using parameter set B. The straight lines are a guide to the eye in order to visualize the level crossing.

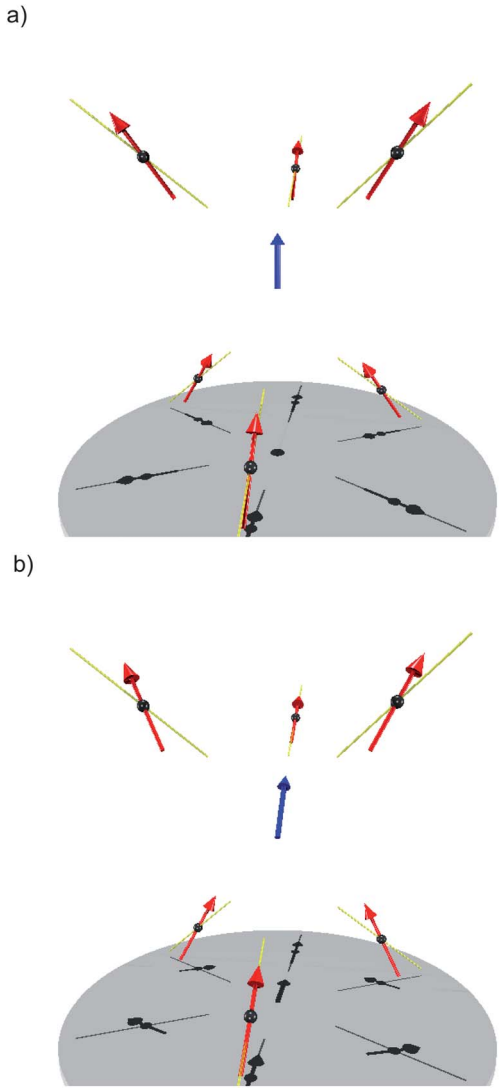

Fig. 18 Classical ground state of $[Mn^{III}_6Mn^{III}]^{3+}$ as obtained by spin dynamics simulations with parameter set B at $T = 0$ K with an external field of 8 T applied in two different directions, namely (a) exactly along the molecular S_6 axis, and (b) oriented at 40° to the molecular S_6 axis, *i.e.* in the direction of the anisotropy axes of two terminal Mn^{III} ions. The blue arrows represent the external magnetic field.

filtered. A solution of D,L-Na(lac) (1005 mg, 8.968 mmol) in methanol (12 mL) was added to the filtrate. The reaction mixture was stirred at room temperature for 30 minutes and filtered again. Slow evaporation of the solvent from the filtrate afforded brown crystals. Yield: 147 mg (45%). ESI-MS(+) (MeOH): *m/z*: 917.0 $[\{(talen^{t\text{-}Bu_2})Mn_3\}_2\{Mn(CN)_6\}]^{3+}$, 1375.8 $[\{(talen^{t\text{-}Bu_2})Mn_3\}_2\{Mn(CN)_6\}]^{2+}$. ESI-MS(−) (MeOH): *m/z*: 89.0 $(lac)^-$, 178.8 $(lac + H(lac))^-$. MALDI-TOF-MS(+) (matrix DCTB): *m/z*: 2751.8 $[\{(talen^{t\text{-}Bu_2})Mn_3\}_2\{Mn(CN)_6\}]^+$, 1428.3 $[\{(talen^{t\text{-}Bu_2})Mn_3\}\{Mn(CN)_4\}]^+$, 1402.2 $[\{(talen^{t\text{-}Bu_2})Mn_3\}\{Mn(CN)_3\}]^+$. IR (KBr): $\tilde{\nu}$ (cm^{-1}) = 2957m, 2907m, 2870m, 2133w, 1613s, 1570s, 1535s, 1491vs, 1437m, 1393m, 1364m, 1341m, 1312m, 1275s, 1254s, 1188m, 1157m, 1092w, 1061w, 1026w, 845m, 818w, 781w, 750w, 642w, 606w, 575m, 550m. Elemental analysis (%): calcd for $[\{(talen^{t\text{-}Bu_2})(Mn^{III}(MeOH))_3\}_2\{Mn^{III}(CN)_6\}](lac)_3 \cdot 3.5MeOH \cdot 3H_2O$ ($C_{162.5}H_{251}N_{18}O_{33.5}Mn_7$): C 57.79, H 7.49, N 7.46; found: C 57.46, H 7.22, N 7.86.

X-Ray crystallography

Brown crystals of **1** were removed from the mother liquor, coated with paraffin oil and immediately cooled to 100(2) K on a Bruker Kappa APEX II diffractometer (four circle goniometer, $Mo_{k\alpha}$ radiation ($\lambda = 0.71073$ Å), focusing graphite monochromator). Empirical absorption corrections using equivalent reflections were performed with the program SADABS 2008/1.[54] The structure was solved with the program SHELXS-97[55] and refined using SHELXL-97.[55] Crystal data for **1**: $C_{169.5}H_{273}Mn_7N_{18}O_{37.5}$, $M = 3547.64$ g mol^{-1}, hexagonal, space group $R\bar{3}$, crystal size $0.40 \times 0.35 \times 0.08$ mm^3, $a = 32.152(3)$, $c = 31.611(3)$ Å, $V = 28\,300(5)$ $Å^3$, $Z = 6$, $\rho_{calcd} = 1.249$ g cm^{-3}, $\mu = 0.526$ mm^{-1}, $2\theta_{max} = 50.00°$, 145 699 reflections measured, 11 055 independent reflections, $R_{int} = 0.0266$, $R = 0.0551$, $wR2 = 0.1458$ (9460 reflections with $I > 2\sigma(I)$), GOF on F^2 1.129, max/min residual electron density 0.931/−0.633 e × $Å^{-3}$.

Other physical measurements

Infrared spectra (400–4000 cm^{-1}) of solid samples were recorded on a Shimadzu FT-IR 8400S as KBr disks. ESI and MALDI-TOF mass spectra were recorded on a Bruker Esquire 3000 ion trap mass spectrometer and a PE Biosystems Voyager DE mass spectrometer, respectively. Elemental analyses were carried out on a LECO CHN-932 or a HEKAtech Euro EA elemental analyzer. Magnetic measurements on bulk samples were performed using a SQUID magnetometer (MPMS XL-7 EC or MPMS-7 or MPMS-5, Quantum Design). Temperature-dependent magnetic susceptibilities were measured in a static field of 1 T in the range 2–290 K. Field-dependent magnetizations were measured at 1.8 K in the range 0–5 T. Variable-temperature variable-field (VTVH) measurements were performed in static fields of 1, 4, and 7 T in the range 2–260 K with the magnetization equidistantly sampled on a $1/T$ temperature scale. For calculations of the molar magnetic susceptibilities, χ_m, the measured susceptibilities were corrected for the underlying diamagnetism of the sample holder and the sample by using tabulated Pascal's constants. AC susceptibilities were measured in the range 1.8–5.0 K in zero static field with an AC field of 3 Oe oscillating at frequencies in the range 660–1500 Hz. Measurements on microgram-sized single-crystals were performed using a home-made micro-Hall-bar magnetometer. The core device of this system, *i.e.* the magnetic sensor, is composed of an array of 10 × 10 μm^2 sized GaAs/GaAlAs 2DEG Hall bars. The cryostat is a ^{3}He Heliox system from Oxford Instruments with a base temperature of 280 mK. Measurements up to 2 T were performed with a 2 T NiTi magnet. For the high-field measurements, a NbTi/Nb_3Sn hybrid magnet with a maximum field of 14 T at 4.2 K and 17 T at 2.1 K was used. A *LakeShore* four quadrant current supply powered both magnets. The sample was oriented in the magnetic field by a mechanical rotator. Special care has been taken in the design of the sample holder in order to minimize heating effects due to eddy currents. To achieve an accurate parallel alignment of the sensor with respect to the magnetic field,

a precision two-axis system was used. This unique system enables high-precision magnetization measurements down to mK temperatures and, especially, in magnetic fields up to 17 T without significant background from the 17 T magnet.

Computational details

***Ab initio* calculations.** All *ab initio* calculations were performed with the MOLCAS 7.4 program package. All employed basis sets were taken from the ANO-RCC basis library available from MOLCAS. The following basis sets were employed for the core $[Mn^{III}(CN)_6]^{3-}$: Mn 7s6p4d3f2g1h; C, N 4s3p2d1f.

The calculations for the central Mn^{III} were done in four structural approximations denoted A, B, C, and D based on the experimental molecular structure. In approximations A and B (Fig. S2A†), the calculated fragment consisted of $[Mn^{III}(C{\equiv}N{-}Mn^{III})_6]^{15+}$. The approximations differ in the way the surrounding six Mn^{III} ions were treated in the *ab initio* calculation: by an AIMP for Mn^{III} (approximation A) or by an all-electron basis set (approximation B), or neglecting the terminal Mn^{III} ions (approximation C, Fig. S2B†). In the last approximation (D), the complete trication $\mathbf{[Mn^{III}_6Mn^{III}]^{3+}}$ except for some of the substituents of the ligand backbone, *e.g.* the *t*-Bu groups, that have been replaced by hydrogen atoms (Fig. S3†), was taken into account in the *ab initio* calculation.

In approximation A, the terminal Mn^{III} were treated by an *ab inito* model potential for Mn^{III}: Mn.ECP.deGraaf.0s.0s.0e–Mn(LaMnO3). In approximation B, the terminal Mn^{III} were treated by an all-electron basis set for Zn^{II}: Zn.ANO-RCC–6s5p3d2f1g. In approximation C, the terminal Mn^{III} were neglected. In approximation D, the terminal Mn^{III} were treated by an all-electron basis set for Zn^{II}: Zn.ANO-RCC–6s5p3d2f1g. Smaller basis sets were employed for the distant atoms: O.ANO-RCC…3s2p (for oxygen atoms bound to the terminal Mn^{III}); N.ANO-RCC…3s2p (for nitrogen atoms bound to the terminal Mn^{III}); C.ANO-DK3.Tsuchiya.12s8p.2s1p (for all carbon atoms); H.ANO-DK3.Tsuchiya.6s.1s (for all hydrogen atoms).

The active space of the Complete Active Space Self Consistent Field (CASSCF) method consisted of four d-type electrons from the last shell of the Mn^{III} spanning five 3d orbitals, and another set of five orbitals to account for the double shell effect, seen for many 3d metals, resulting in CAS (4 in 10). The complete active space second order correction to the energies (CASPT2) was possible to perform only for approximations A and C. The spin-orbit coupling was performed by the restricted active space state interaction (RASSI) method. All states arising from ligand field transitions were taken into the spin-orbit mixing: 5 quintets, 45 triplets and 50 singlets.

Quantum spin-Hamiltonian simulations. The magnetic properties of $\mathbf{[Mn^{III}_6Mn^{III}]^{3+}}$ were simulated by a full-matrix diagonalization of the spin-Hamiltonian in eqn (1).

$$\hat{\mathbf{H}} = -2\sum_{i<j} J_{ij}\hat{\mathbf{S}}_i\cdot\hat{\mathbf{S}}_j + \sum_i D_i\left(\hat{\mathbf{S}}_i\cdot\mathbf{e}_i(\vartheta_i,\varphi_i)\right)^2 + \mu_B\sum_i \mathbf{B}\cdot\underline{\underline{\mathbf{g}}}_i\cdot\hat{\mathbf{S}}_i \quad (1)$$

Here the first sum reflects the isotropic exchange interaction between spins given by the spin vector operators $\hat{\mathbf{S}}_i$ at sites *i*. The anisotropic magnetization behavior of the individual ions is accounted for by local anisotropy tensors in the second sum. The tensors are parameterized by a strength factor $D_i = D$ as well as local unit vectors $\mathbf{e}_i$, which are parameterized by polar angles ϑ_i and φ_i. They represent an easy or a hard axis depending on the sign of *D*. For the six terminal Mn^{III} ions the unit vectors point along the local Jahn–Teller axes. Due to the S_6 symmetry all six local unit vectors $\mathbf{e}_i$ can be parameterized by the common polar angle between the Jahn–Teller axes and the S_6 symmetry axis, which has been extracted from the crystal structure and is $\vartheta = 37.5°$. The relative φ_i angles are determined by the S_6 symmetry. The central Mn^{III} is treated as a diamagnetic $S_i = 0$ ion. The third term of the Hamiltonian models the interaction with the applied magnetic field. $\underline{\underline{\mathbf{g}}}_i$ represents the local g-matrix at site *i*. For the terminal Mn^{III} ions an isotropic value of 1.98 is assumed. The Hilbert space of the full spin-Hamiltonian has a dimension of 15 625. In the presence of a magnetic field we employ inversion symmetry. This reduces the average matrix size to roughly half the full size. Since the measurements are performed on ensembles of small crystallites we also employ an orientational average using an isotropic grid with 20 orientations.[27,52]

In order to compare with single-crystal magnetization measurements, we also evaluated the magnetization function along certain crystallographic directions. This allows us to reproduce the step-like behavior seen in the double hysteresis loops. But since the calculations are done for equilibrium situations, the hysteretic behavior itself cannot be modelled. For this purpose a quantum master equation would have to be solved, which is out of reach for a spin system as large as this one.[56]

Classical spin dynamics simulations. The Hamiltonian of the classical system is written as

$$\hat{H}_c = -2\sum_{i<j} J^c_{ij}\vec{m}_i\cdot\vec{m}_j + \sum_i D^c_i(\vec{m}_i\cdot\vec{e}_i(\vartheta_i,\varphi_i))^2 + \mu_c\sum_i \mathbf{B}\cdot\vec{m}_i \quad (2)$$

The spins $\vec{m}_i$ are classical unit vectors. The Hamiltonian of eqn (2) provides the classical counterpart to the quantum Heisenberg model in eqn (1). This correspondence is achieved by replacing in eqn (1) all quantum spin operators according to $\hat{\mathbf{S}}_k = \sqrt{s_k(s_k+1)}\cdot\vec{m}_k$ with s_k describing the spin quantum number of a given ion.[57] It thus follows that $J^c_{kl} = \sqrt{s_k(s_k+1)s_l(s_l+1)}\cdot J_{kl}$ and $D^c_k = s_k(s_k+1)\cdot D_k$; moreover the quantity μ_c in eqn (2) is given by $\mu_c = (g_k\mu_B)\sqrt{s_k(s_k+1)}$ where g_k is the Landé *g* factor for the given ion and μ_B is the Bohr magneton. We have checked the applicability of our classical treatment by comparing the results of classical Monte Carlo calculations with the exact quantum model calculations described above.

Furthermore we have studied the low-temperature field-dependent spin dynamics. An effective method for investigating this property is to use the numerical solution of the stochastic Landau–Lifshitz equation which simulates the time evolution of the spin system coupled to a heat bath. Fluctuating fields with white noise characteristics are used to account for the effects of the interaction of the spin system with the heat bath. Those environmental degrees of freedom are also responsible for the damped precession of the magnetization parameterized by a phenomenological damping factor.[57,58]

Conclusion

We have synthesized the triplesalen complex $[Mn^{III}_6Mn^{III}]^{3+}$. The triplesalen ligand enforces a molecular C_3 symmetry, while the Mn^{III} salen-like coordination environment provides a strong source of local magnetic anisotropy D_i originating from second-order spin orbit coupling. In order to enhance the magnetic properties compared to our first reported $[Mn^{III}_6Cr^{III}]^{3+}$ single-molecule magnet,[26] we incorporated a source of first-order orbital angular momentum by substituting the central hexacyanochromate with hexacyanomanganate, which features a Mn^{III} l.s. ion. As the $[Mn^{III}_6Cr^{III}]^{3+}$ SMM with BPh_4^- as counterion crystallizes in a low-symmetry space group,[26] we used the rod-shaped anion lactate to enforce the crystallization of $[Mn^{III}_6Mn^{III}](lac)_3$ in a highly symmetric space group. Indeed, $[Mn^{III}_6Mn^{III}](lac)_3$ crystallizes in the space group $R\bar{3}$. This has important consequences for the molecular and crystal symmetry: 1) In contrast to the $[Mn^{III}_6Cr^{III}]^{3+}$ complex, which is only approximately C_3 symmetric, the $[Mn^{III}_6Mn^{III}]^{3+}$ complex possesses crystallographic S_6 symmetry. 2) The molecular S_6 axes of the $[Mn^{III}_6Mn^{III}]^{3+}$ molecules are all aligned in one direction in the crystal structure of $[Mn^{III}_6Mn^{III}](lac)_3$. 3) The surroundings of each $[Mn^{III}_6Mn^{III}]^{3+}$ cation in the crystal structure are more symmetric, which leads to less perturbation of the molecular symmetry.

Single-crystals of $[Mn^{III}_6Mn^{III}](lac)_3$ exhibit a double hysteresis with an opening up to 1.8 T for the spin ground state and an opening up to 10 T for an excited state, which becomes ground state at $\approx$ 3.4 T. We are not aware of a hysteretic opening of a SMM at such high magnetic fields. A combined theoretical study including *ab initio* calculations taking into account spin-orbit coupling, quantum mechanical, and classical spin-Hamiltonian simulations provides a clear understanding of this double hysteresis.

The *ab initio* calculations at the CASSCF and CASPT2 level establish that the central Mn^{III} l.s. of $[Mn^{III}_6Mn^{III}]^{3+}$ experiences spin-orbit coupling of the effective $\tilde{L} = 1$ and the spin $S = 1$ resulting in a diamagnetic $\tilde{J} = 0$ ground state separated from $\tilde{J} = 1$ and $\tilde{J} = 2$ excited multiplets, which become populated only at higher temperatures. It should be noted that predictions from approximate ligand-field theory are not always supported by the more sophisticated *ab initio* calculations. As an example one could mention the complex $[Mo^{III}(CN)_7]^{4-}$, for which the order of low-lying levels obtained *via ab initio* CASSCF/CASPT2 calculations could not be reproduced by a standard angular overlap model for any parameters.[59] A careful analysis has shown that the reason for this discrepancy is the different value of the isotropic bielectronic parameter A in different orbitals of the complex. This effect is of purely covalent nature and cannot be taken into account by ligand-field theory, which in any of its versions involves spherically symmetric bielectronic interactions described by three Racah parameters A, B, and C. Deviations from the predictions of ligand-field theory due to covalency effects have also been found recently in our *ab initio* investigations of Os^{IV} complexes. The results of our *ab initio* calculations for $[Mn^{III}_6Mn^{III}]^{3+}$ imply that, despite the important contribution of the $[Mn^{III}(CN)_6]^{3-}$ building block to the magnetic properties of other molecule-based magnets,[40–43,60,61] the hexacyanomanganate in $[Mn^{III}_6Mn^{III}]^{3+}$ does not contribute to the low-temperature magnetism. This results from the more than half-filled t_{2g} shell of the Mn^{III} ion, which yields a positive value for the spin-orbit coupling constant irrespective of the molecular symmetry. In order to further optimize our heptanuclear single-molecule magnets, the incorporation of d^2 hexacyanometallates seems valuable.

The non-magnetic nature of the central Mn^{III} ion further entails that there are no Mn^{III}(central)–Mn^{III}(terminal) exchange couplings, which appears to be the main reason for the low blocking temperature T_B of $[Mn^{III}_6Mn^{III}]^{3+}$. The ground state at zero magnetic field is well described by an up-up-down alignment of the three Mn^{III} spins in a trinuclear triplesalen subunit. The orientation of the local Mn^{III} **D**-tensors at an angle $\vartheta = 37.5°$ relative to the molecular S_6 axis results in a merely small anisotropy barrier, which causes the hysteresis between −1.8 and +1.8 T at 0.3 K.

At fields >2 T, the ground state changes to an all-up orientation of the local Mn^{III} spins. Interestingly, due to the weak-exchange limit in $[Mn^{III}_6Mn^{III}]^{3+}$, the main part of the Zeeman energy required for the spin-flip is needed to overcome the local anisotropy barriers, and only minor contributions are required to overcome the antiferromagnetic exchange.

In conclusion, the special spin topology in combination with the high molecular and crystal symmetry allows the observation of a hysteretic opening for a single-molecule magnet up to 10 T.

Acknowledgements

This work was supported by the Fonds der Chemischen Industrie and the DFG (FOR945 "Nanomagnets"). V.H. also gratefully acknowledges the Fonds der Chemischen Industrie for a doctoral fellowship. We are grateful to Professor Arndt Simon (Max Planck Institute for Solid State Research, Stuttgart) for his advice regarding rod packings.

References

1 R. Sessoli, D. Gatteschi, A. Caneschi and M. A. Novak, *Nature*, 1993, **365**, 141–143.
2 D. Gatteschi and R. Sessoli, *Angew. Chem., Int. Ed.*, 2003, **42**, 268–297.
3 D. Gatteschi, R. Sessoli and J. Villain, *Molecular Nanomagnets*, Oxford University Press, Oxford, 2006.
4 G. Christou, D. Gatteschi, D. N. Hendrickson and R. Sessoli, *MRS Bull.*, 2000, **25**, 66–71.
5 L. Thomas, F. Lionti, R. Ballou, D. Gatteschi, R. Sessoli and B. Barbara, *Nature*, 1996, **383**, 145–147.
6 A. Dei and D. Gatteschi, *Angew. Chem., Int. Ed.*, 2011, **50**, 11852–11858.
7 J. Tejada, *Polyhedron*, 2001, **20**, 1751–1756.
8 J. Tejada, E. M. Chudnovsky, E. del Barco, J. M. Hernandez and T. P. Spiller, *Nanotechnology*, 2001, **12**, 181–186.
9 D. D. Awschalom, D. P. Di Vincenzo and J. J. Smyth, *Science*, 1992, **258**, 414–421.
10 M. N. Leuenberger and D. Loss, *Nature*, 2001, **410**, 789–793.
11 A. Cornia, A. C. Fabretti, M. Pacchioni, L. Zobbi, D. Bonacchi, A. Caneschi, D. Gatteschi, R. Biagi, U. Del Pennino, V. De Renzi, L. Gurevich and H. S. J. Van der Zant, *Angew. Chem., Int. Ed.*, 2003, **42**, 1645–1648.
12 C. J. Wedge, G. A. Timco, E. T. Spielberg, R. E. George, F. Tuna, S. Rigby, E. J. L. McInnes, R. E. P. Winpenny, S. J. Blundell and A. Ardavan, *Phys. Rev. Lett.*, 2012, **108**, 107204.
13 G. A. Timco, S. Carretta, F. Troiani, F. Tuna, R. J. Pritchard, C. A. Muryn, E. J. L. McInnes, A. Ghirri, A. Candini, P. Santini, G. Amoretti, M. Affronte and R. E. P. Winpenny, *Nat. Nanotechnol.*, 2009, **4**, 173–178.
14 C.-F. Lee, D. A. Leigh, R. G. Pritchard, D. Schultz, S. J. Teat, G. A. Timco and R. E. P. Winpenny, *Nature*, 2009, **458**, 314–318.

15 J. Liu, E. del Barco and S. Hill, *Phys. Rev. B: Condens. Matter Mater. Phys.*, 2012, **85**, 012406.
16 H. C. Longuet-Higgins, *J. Chem. Phys.*, 1950, **18**, 265–274.
17 H. M. McConnell, *J. Chem. Phys.*, 1963, **39**, 1910.
18 I. Fernández, R. Ruiz, J. Faus, M. Julve, F. Lloret, J. Cano, X. Ottenwaelder, Y. Journaux and C. Munoz, *Angew. Chem., Int. Ed.*, 2001, **40**, 3039–3042.
19 E. Pardo, R. Ruiz-Garcia, J. Cano, X. Ottenwaelder, R. Lescouezec, Y. Journaux, F. Lloret and M. Julve, *Dalton Trans.*, 2008, 2780–2805.
20 T. Glaser, M. Gerenkamp and R. Fröhlich, *Angew. Chem., Int. Ed.*, 2002, **41**, 3823–3825.
21 T. Glaser, M. Heidemeier, S. Grimme and E. Bill, *Inorg. Chem.*, 2004, **43**, 5192–5194.
22 T. Glaser, M. Heidemeier, J. B. H. Strautmann, H. Bögge, A. Stammler, E. Krickemeyer, R. Huenerbein, S. Grimme, E. Bothe and E. Bill, *Chem.–Eur. J.*, 2007, **13**, 9191–9206.
23 H. Theil, C.-G. Freiherr von Richthofen, A. Stammler, H. Bögge and T. Glaser, *Inorg. Chim. Acta*, 2008, **361**, 916–924.
24 T. Glaser, *Chem. Commun.*, 2011, **47**, 116–130.
25 T. Glaser, M. Heidemeier, R. Fröhlich, P. Hildebrandt, E. Bothe and E. Bill, *Inorg. Chem.*, 2005, **44**, 5467–5482.
26 T. Glaser, M. Heidemeier, T. Weyhermüller, R.-D. Hoffmann, H. Rupp and P. Müller, *Angew. Chem., Int. Ed.*, 2006, **45**, 6033–6037.
27 T. Glaser, M. Heidemeier, E. Krickemeyer, H. Bögge, A. Stammler, R. Fröhlich, E. Bill and J. Schnack, *Inorg. Chem.*, 2009, **48**, 607–620.
28 E. Krickemeyer, V. Hoeke, A. Stammler, H. Bögge, J. Schnack and T. Glaser, *Z. Naturforsch.*, 2010, **65b**, 295–303.
29 O. Waldmann, *Inorg. Chem.*, 2007, **46**, 10035–10037.
30 F. Neese and D. A. Pantazis, *Faraday Discuss.*, 2011, **148**, 229–238.
31 J. D. Rinehart, M. Fang, W. J. Evans and J. R. Long, *J. Am. Chem. Soc.*, 2011, **133**, 14236–14239.
32 J. D. Rinehart, M. Fang, W. J. Evans and J. R. Long, *Nat. Chem.*, 2011, **3**, 538–542.
33 N. Ishikawa, M. Sugita, T. Ishikawa, S. Koshihara and Y. Kaizu, *J. Am. Chem. Soc.*, 2003, **125**, 8694–8695.
34 S. Takamatsu, T. Ishikawa, S. Koshihara and N. Ishikawa, *Inorg. Chem.*, 2007, **46**, 7250–7252.
35 M. Gonidec, F. Luis, À. Vílchez, J. Esquena, D. B. Amabilino and J. Veciana, *Angew. Chem., Int. Ed.*, 2010, **49**, 1623–1626.
36 M. Gonidec, R. Biagi, V. Corradini, F. Moro, V. De Renzi, U. del Pennino, D. Summa, L. Muccioli, C. Zannoni, D. B. Amabilino and J. Veciana, *J. Am. Chem. Soc.*, 2011, **133**, 6603–6612.
37 M. Kotani, *J. Phys. Soc. Jpn.*, 1949, **4**, 293–297.
38 W. E. Buschmann, L. Liable-Sands, A. L. Rheingold and J. S. Miller, *Inorg. Chim. Acta*, 1999, **284**, 175–179.
39 W. E. Buschmann, J. Ensling, P. Gütlich and J. S. Miller, *Chem.–Eur. J.*, 1999, **5**, 3019–3028.
40 C. P. Berlinguette, D. Vaughn, C. Canada-Vilalta, J. R. Galan-Mascaros and K. R. Dunbar, *Angew. Chem., Int. Ed.*, 2003, **42**, 1523–1526.
41 A. V. Palii, S. M. Ostrovsky, S. I. Klokishner, B. S. Tsukerblat, C. P. Berlinguette, K. R. Dunbar and J. R. Galán-Mascarós, *J. Am. Chem. Soc.*, 2004, **126**, 16860–16867.
42 W. Kaneko, S. Kitagawa and M. Ohba, *J. Am. Chem. Soc.*, 2007, **129**, 248–249.
43 W. Kaneko, M. Mito, S. Kitagawa and M. Ohba, *Chem.–Eur. J.*, 2008, **14**, 3481–3489.
44 M. O'Keeffe and S. Andersson, *Acta Crystallogr., Sect. A: Cryst. Phys., Diffr., Theor. Gen. Crystallogr.*, 1977, **A33**, 914–923.
45 S. Andersson and M. O'Keeffe, *Nature*, 1977, **267**, 605–606.
46 F. Livolant, A. M. Levelut, J. Doucet and J. P. Benoit, *Nature*, 1989, **339**, 724–726.
47 A. Thess, R. Lee, P. Nikolaev, H. Dai, P. Petit, J. Robert, C. Xu, Y. H. Lee, S. G. Kim, A. G. Rinzler, D. T. Colbert, G. E. Scuseria, D. Tománek, J. E. Fischer and R. E. Smalley, *Science*, 1996, **273**, 483–487.
48 M. C. Schaloske, L. Kienle, H. Mattausch, V. Duppel and A. Simon, *Eur. J. Inorg. Chem.*, 2011, 4049–4056.
49 J.-J. Girerd and Y. Journaux, in *Physical Methods in Bioinorganic Chemistry*, ed. L. J. Que, University Science Books, Sausalito, 2000, pp. 321–374.
50 A. Abragam and B. Bleaney, *Electron Paramagnetic Resonance of Transition Ions*, Clarendon Press, Oxford, GB, 1970.
51 V. S. Mironov, L. F. Chibotaru and A. Ceulemans, *J. Am. Chem. Soc.*, 2003, **125**, 9750–9760.
52 J. Schnack, *Condens. Matter Phys.*, 2009, **12**, 323–330.
53 T. Glaser, M. Heidemeier and T. Lügger, *Dalton Trans.*, 2003, 2381–2383.
54 G. M. Sheldrick, *SADABS 2008/1*, University of Göttingen, Göttingen, Germany, 2008.
55 G. M. Sheldrick, *Acta Crystallogr., Sect. A: Found. Crystallogr.*, 2008, **A64**, 112–122.
56 T. Kawakami, H. Nitta, M. Takahata, M. Shoji, Y. Kitagawa, M. Nakano, M. Okumura and K. Yamaguchi, *Polyhedron*, 2009, **28**, 2092–2096.
57 L. Engelhardt and C. Schröder, in *Molecular Cluster Magnets*, ed. R. E. P. Winpenny, World Scientific Publishers, Singapore, 2011.
58 V. P. Antropov, S. V. Tretyakov and B. N. Harmon, *J. Appl. Phys.*, 1997, **81**, 3961–3965.
59 L. F. Chibotaru, M. F. A. Hendrickx, S. Clima, J. Larionova and A. Ceulemans, *J. Phys. Chem. A*, 2005, **109**, 7251–7257.
60 B. S. Tsukerblat, A. V. Palii, S. M. Ostrovsky, S. V. Kunitsky, S. I. Klokishner and K. R. Dunbar, *J. Chem. Theory Comput.*, 2005, **1**, 668–673.
61 C. M. Kareis, S. H. Lapidus, J.-H. Her, P. W. Stephens and J. S. Miller, *J. Am. Chem. Soc.*, 2012, **134**, 2246–2254.

